Rapid #: -20197508

CROSS REF ID: **2149617**

LENDER: **LHL4CRLRM :: Main Library**

BORROWER: **WAU :: Suzzallo Library**

TYPE:	Article CC:CCG
JOURNAL TITLE:	Rare Metals
USER JOURNAL TITLE:	Rare Metals
ARTICLE TITLE:	Trivalent Ni oxidation controlled through regulating lithium content to minimize perovskite interfacial recombination
ARTICLE AUTHOR:	Zhao, Jin-Jin
VOLUME:	41
ISSUE:	1
MONTH:	
YEAR:	2022
PAGES:	96-105
ISSN:	1001-0521
OCLC #:	

Processed by RapidX: 2/1/2023 2:40:45 PM

Rare Met. (2022) 41(1):96–105
https://doi.org/10.1007/s12598-021-01800-6

RARE METALS

ORIGINAL ARTICLE

Trivalent Ni oxidation controlled through regulating lithium content to minimize perovskite interfacial recombination

Jin-Jin Zhao*, Xiao Su, Zhou Mi, Ying Zhang, Yan-Jun Hu*, Hua-Jun Guo, Yi-Nan Jiao, Yu-Xia Zhang, Yan Shi, Wei-Zhong Hao, Jing-Wei Wu, Yi Wang, Cun-Fa Gao*, Guo-Zhong Cao

Received: 26 February 2021 / Revised: 23 April 2021 / Accepted: 13 May 2021 / Published online: 28 August 2021

Abstract Organic–inorganic hybrid perovskite solar cells, one of the most promising photovoltaic devices, have made great progress in their efficiency and preparation technology. In this study, uniform, highly conductive Li_nNiO_x ($0 \le n \le 1$; $0 < x \le 3$) films were prepared by electrochemical deposition for a range of Li concentration. Photovoltaic performance for the perovskite solar cells was enhanced through incorporation of the ion pair of $Ni^{3+} \leftrightarrow Ni^{2+}$ as the interfacial passivation. Depending on the amount of lithium doping, controlled interfacial oxidation was induced by Ni^{3+}. The $Li_{0.32}NiO_x$ inhibited charge recombination, reduced the defect density, and enhanced the photocurrent density. A maximum power conversion efficiency of 20.44% was obtained by $Li_{0.32}NiO_x$. Further, in the long-term, in-air stabilities of unencapsulated Li_nNiO_x perovskite solar cells were demonstrated.

Keywords Lithium ions; Ni^{3+}; Oxidized defect; Photocurrent; Perovskite solar cells

1 Introduction

Perovskite electronic devices have been attracted considerable attentions for wearable, intelligent, and scalable development [1, 2], due to their high light absorption coefficient, long carrier life, high carrier mobility, and tunable bandgap [1, 3]. Regulation of oxidized perovskite has been conducted to improve the power conversion efficiency (PCE) and device's long-term durability [4, 5]. Environmental illumination/heating accelerates the degradation of perovskite layers, causing oxidation of I^- to I^0 [5] and Pb^{2+} reduction to metallic Pb^0 [6–8]. Zhou et al. showed that the europium ion pair Eu^{3+}–Eu^{2+} acted as the "redox shuttle" that selectively oxidized Pb^0 and reduced I^0 defects simultaneously in a cyclical transition [4]. Wang et al. [5] reported that I^- was easily oxidized to I^0, which not only served as carrier recombination centers but also initiated chemical chain reactions to accelerate the degradation of perovskite layers. Several attempts have been devoted to eliminating either Pb^0 or I^0 defects, including optimizing film processing [9] and additive engineering [4, 10]. To date, these additives are mostly sacrificial

Jin-Jin Zhao, Xiao Su, Zhou Mi and Ying Zhang contributed equally to this work.

Supplementary Information The online version contains supplementary material available at https://doi.org/10.1007/s12598-021-01800-6.

J.-J. Zhao*, X. Su, Z. Mi, Y. Zhang, H.-J. Guo, Y.-N. Jiao, Y.-X. Zhang, W.-Z. Hao, J.-W. Wu, Y. Wang
School of Materials Science and Engineering, School of Mechanical Engineering, Shijiazhuang Tiedao University, Shijiazhuang 050043, China
e-mail: jinjinzhao2012@163.com

Y.-J. Hu*
School of Materials Science and Engineering, Hebei Key Laboratory of Material Near Net Forming Technology, Hebei University of Science and Technology, Shijiazhuang 050018, China
e-mail: hubluce@163.com

Y. Shi, C.-F. Gao*
State Key Laboratory of Mechanics and Control of Mechanical Structures, Nanjing University of Aeronautics and Astronautics, Nanjing 210016, China
e-mail: cfgao@nuaa.edu.cn

G.-Z. Cao
Department of Materials Science and Engineering, University of Washington, Seattle, WA 98195-2120, USA

agents for perovskite, which diminish soon after their militating. Operational durability requires the simultaneous elimination of interfacial oxidized/reduced defects between charge carrier transport layer (TL) and perovskite layer in devices in a sustainable manner.

The strategy for elimination interfacial oxidized/reduced defects in device is modification of the hole transport layer (HTL)/perovskite interface. NiO_x is widely used as HTL in perovskite solar cells [11–14], due to enhanced charge transport dynamics, suppressed charge recombination [15], and fewer surface trap states compared with the widely styrene sulfonic acid used poly(3,4-ethylenedioxythiophene)/poly(styrenesulfonic acid) (PEDOT/PSS) hole-transporting layer [16]. However, pure NiO_x without doping exhibits a wide direct bandgap of 3.5–4.0 eV, low p-type conductivity, and high recombination rate during extraction and transportation [17, 18]. Chen et al. [3] revealed that the recombination time of NiO_x HTL was completed at the sub-picosecond time scale, whereas the recombination time between the injected holes in NiO_x and mobile electrons in perovskites ranged from hundreds of picoseconds to a few of nanoseconds via time-resolved terahertz spectroscopy [19]. Poor photovoltaic performance for pure NiO_x HTL can be attributed to the following two reasons. (1) The NiO_x holes are pinned at the surface, where the interfacial recombination rate increases by the reducing electrons [20]. (2) The strong dipole/polarization of the NiO_x composite film induces adhesion of perovskite precursor ions on the surface of NiO_x during the perovskite film formation and creates defects at the interface [21]. The nickel element has two valent states of bivalent (+2) and trivalent (+3) states [22, 23]. To alleviate NiO_x HTL/perovskite interfacial defects caused by NiO_x dipole/polarization, the additive ions were intentionally inserted into NiO_x lattice to precisely control the Ni^{2+}/Ni^{3+} ratio [17]. Additive doping NiO_x film with high optical transparency and stability plays a key role in the efficient extraction of holes and the prevention of electron leakage in a perovskite solar cell (PSC) [17]. Similar ionic radii of Ni^{2+} were believed to minimize the mismatch and enhance the lattice stability, which has already been proved by effective Li dopants, because of the similar radius $R(Li^+)$ = (0.072–0.076 nm), and $R(Ni^{2+}$or $Ni^{3+})$ = (0.069–0.074 nm) [24, 25], whereas monovalent lithium (Li) doping in NiO_x improves the conductivity efficiently [3, 19].

To eliminate perovskite oxidized defects caused by Ni^{3+}, it is essential that additive Li^+ is intentionally inserted into NiO_x lattice to precisely control the Ni^{2+}/Ni^{3+} ratio. Appropriate Ni^{3+}-doped NiO_x as HTL will improve photovoltaic performance in perovskite solar cells [26]. Traore et al. [27] calculated that Li doping in NiO_x improved energy alignment of the perovskite–NiO_x interface and enhanced hole extraction by DFT. Qiu et al. [28] reported that HTL electrical conductivity was enhanced by Li pulse laser deposited on NiO_x films. To uniformly distribute nano-sized Li onto NiO_x, electrochemical deposition enables the reduction of metal precursors within a very short time period (~0.1 s), thus allowing the formation of nano-sized metallic Li clusters without large aggregation at low potential [29]. The electrochemical deposition method exhibits the advantages of uniformity and high quality in NiO_x hole transport film fabrication [30–32]. However, the accurate elemental doping proportions in hole transfer layer (HTL) have been overlooked to date. The accurate Li^+ doping in the hole transport layer and the Ni^{3+} contents on oxidation was rarely investigated for PSCs.

We demonstrate that accurate trivalent Ni^{3+} ratio in NiO_x hole transfer layer by controlled lithium doping leads to exceptional photocurrent improvement and high PCE through incorporation of the ion pair of $Ni^{3+} \leftrightarrow Ni^{2+}$ as the interfacial passivation. Depending on the amount of lithium doping, controlled interfacial oxidation could be achieved. The $Li_{0.32}NiO_x$ doping inhibited charge recombination, reduced the defect density, and enhanced the photocurrent density.

2 Experimental

2.1 Materials

Nickel nitrate hexahydrate ($Ni(NO_3)_2{\cdot}6H_2O$) (98%), anisole (99.7%), and isopropyl alcohol (IPA) (99.5%) were purchased from Aladdin. Lithium acetate CH_3COOLi (99.95%), N,N-dimethylformamide (DMF) (99.8%), and dimethyl sulfoxide (DMSO) (99.9%) were purchased from Sigma-Aldrich. $HC(NH_2)_2I$ (FAI) (99.5%) and CH_3NH_3Br (MABr) (99.5%) were purchased from Lumtec Co. (Taiwan, China). CsI (99.98%) was purchased from Alfa Aesar. PbI_2 (>99.99%), $PbBr_2$ (>99.99%), [6,6]-phenyl-C61-butyric acid methyl ester ($PC_{61}BM$) (99.5%), and 2,9-dimethyl-4,7-diphenyl-1,10-phenanthroline (BCP) (99%) were purchased from Xi'an Polymer Light Technology Corp. Ethyl alcohol and acetone were purchased from Sinopharm Chemical Reagent Co., Ltd. Fluorine-doped tin oxide (FTO) glass with a sheet resistance of 7 $\Omega{\cdot}square^{-1}$ was purchased from Advanced Election Technology Co., Ltd. Ag (99.99%) was purchased from Mat-cn.

2.2 Li_nNiO_x fabrication

FTO glass substrates were rinsed by sequential ultrasonic treatment in detergent, deionized water, anhydrous ethanol, acetone, and isopropyl alcohol for 20 min and then dried with a nitrogen stream. Then, the substrates were treated with UV-ozone for 20 min in plasma cleaner. Li_nNiO_x was

electrochemically deposited using a constant current mode of three-electrode CHI 660a electrochemical workstation. The three electrodes were FTO glass as the working electrode, the Ag/AgCl electrode as the reference electrode, and the platinum electrode as the counter electrode. 3 mmol of nickel nitrate hexahydrate and lithium acetate in different proportions was dissolved in 30 ml deionized water as deposition solution. The deposition current density was controlled in the range of 0.05–0.50 $mA \cdot cm^{-2}$. After the deposition, the Li_nNiO_x film was rinsed with deionized water and absolute ethanol and then annealed at 300 °C for 1 h at ambient pressure.

2.3 Perovskite solar cell fabrication

The Li_nNiO_x (n = 0, 0.13, 0.24, 0.32, 0.38) film doped with different ratios of lithium was transferred into a glove box filled with N_2 to complete the remaining processes. Precursor solution of $Cs_{0.05}FA_{0.81}MA_{0.14}PbI_{2.55}Br_{0.45}$ (CsFAMA) was prepared in two steps: First, 1.211 $mol \cdot L^{-1}$ FAI and 1.275 $mol \cdot L^{-1}$ PbI_2 were dissolved in a 1:4 volume ratio of DMSO/DMF as Solution (I), 1.425 $mol \cdot L^{-1}$ MABr and 1.5 $mol \cdot L^{-1}$ $PbBr_2$ were dissolved in a 1:4 volume ratio of DMSO/DMF as Solution (II), and 0.75 $mol \cdot L^{-1}$ CsI was dissolved in DMSO as Solution (III). Then, 440 μl Solution (I), 66 μl Solution (II), and 44 μl Solution (III) were mixed and stirred for 12 h at room temperature. The perovskite precursor solution was spin-coated onto glass/FTO/Li_nNiO_x (n = 0, 0.13, 0.24, 0.32, 0.38) substrate under 1000 $r \cdot min^{-1}$ for 10 s and 4000 $r \cdot min^{-1}$ for 60 s. 68 μl anisole was jetted onto the spinning substrate for 30 s, and then, the spin coating was terminated. The film was annealed at 110 °C for 20 min in a nitrogen filled glove box, and then, CsFAMA film on glass/FTO/Li_nNiO_x substrate was obtained. The electron transport layer $PC_{61}BM$ (0.02 $mol \cdot L^{-1}$ $PC_{61}BM$ dissolved in anisole) was spin-coated at 4000 $r \cdot min^{-1}$ for 30 s and annealed at 70 °C for 10 min, and BCP layer (3.5 $mol \cdot L^{-1}$ BCP dissolved in isopropanol) was spin-coated at 5000 $r \cdot min^{-1}$ for 30 s. And 70–80 nm Ag was thermally evaporated under high vacuum onto BCP as top electrode.

2.4 Characterization

X-ray diffractometer (XRD) patterns were obtained using D8 Advance diffractometer with Cu Kα radiation (40 kV and 40 mA) under the scanning rate of 4 (°)·min^{-1} for a wide-angle test over the Bragg angle range of 10°–90°. Scanning electron microscopy (SEM) measurements were performed using a Hitachi-SU8010 electron microscope operated at an acceleration voltage of 5 kV. X-ray photoelectron spectroscopy (XPS) data were measured using Thermo Fisher's ESCALAB250Xi instrument. The steady-state photoluminescence (PL) spectra were measured by the fluorescence spectrometer at Shanghai Anting Electronic Instrument Factory. The photocurrent–voltage (J–V) characteristics of the solar cells were measured using a Keithley 2400. The source was under the illumination of simulated sunlight (AM1.5, 100 $mW \cdot cm^{-2}$) provided by a solar simulator (Newport 69907) with an AM 1.5 filter. Light intensity was adjusted using an NREL-calibrated Si solar cell with a KG-2 filter for approximating 1 sunlight intensity. While measuring current and voltage, the cell was covered with a black mask having an aperture of 0.026 cm^2. Measurement of inductively coupled plasma-optical emission spectroscopy (ICP-OES) for Li_nNiO_x films was performed by an Agilent ICPOES730 instrument. The ultraviolet–visible spectroscopy (UV–Vis) absorption and transmission curves were determined with a Hitachi U-4100. Transmission electron microscopy (TEM) was performed at room temperature with JEOL's JEM-F200 at 200 kV. The time-resolved photoluminescence spectroscopy (TRPL) spectra were recorded with Fls-800 spectrometers.

3 Results and discussion

The electrochemical fabrication process of lithium-doped nickel oxide film (abbreviated as Li_nNiO_x, $0 \le n \le 1$; $0 < x \le 3$) is schematically shown in Fig. 1. To uniformly deposit Li_nNiO_x film on a fluorine-doped tin oxide (FTO) substrate, the deposition mode of a constant current of 1×10^{-4} A is operated in Fig. S1a. The preparation process is as following:

$$H_2O(l) + NO_3^-(aq) + 2e^- \rightarrow 2OH^-(aq) + NO_2^-(aq) \quad (1)$$

which placed the hydroxyl ions on FTO surface [31, 33].

$$nLi^+(aq) + Ni^{x+}(aq) + (x+n)OH^-(aq) \rightarrow nLi(OH)(s) + Ni(OH)_x(s) \rightarrow Li_nNiO_x \quad (2)$$

in which lithium nickel hydroxide reacted lithium/nickel ions with hydroxyl ions, prior to annealing the product to form lithium nickelate.

The perovskite $Cs_{0.05}FA_{0.81}MA_{0.14}PbI_{2.55}Br_{0.45}$ (denoted as CsFAMA), electron transfer layer ($PC_{61}BM$/BCP), and electrode were sequentially fabricated on the hole-transfer layer of Li_nNiO_x, thereby constructing the glass/FTO/Li_nNiO_x/CsFAMA/$PC_{61}BM$/BCP/Ag solar cell.

Figure 2a shows X-ray diffraction (XRD) patterns of Li_nNiO_x ($0 < x \le 3$) layers as a function of Li content (n = 0, 0.13, 0.24, 0.32, 0.38, respectively). Diffraction peaks at 37.78° and 61.63° can be seen in XRD pattern in Fig. 2a, indicating (retrieved PDF No. 47-1049 and PDF No. 26-1175) the (111) crystal plane of NiO_x ($0 < x \le 3$, orthorhombic unit cell) [34] and the (006) crystal plane of

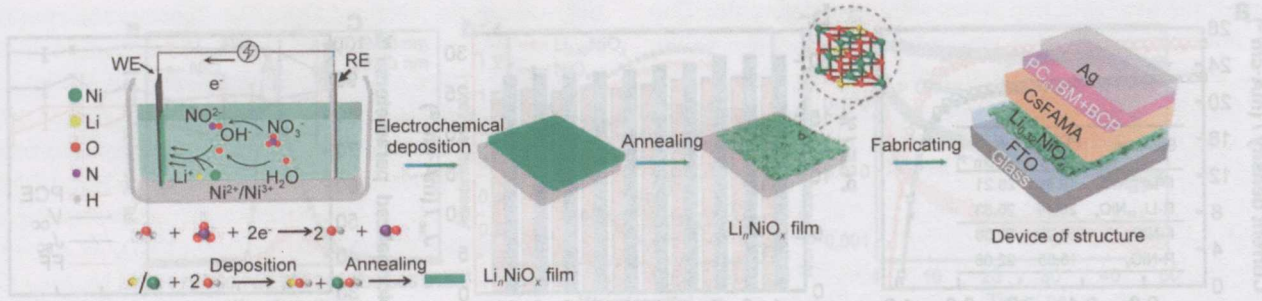

Fig. 1 Schematics illustrating Li_nNiO_x ($0 \le n \le 1$; $0 < x \le 3$) electrochemical device structure of glass/FTO/Li_nNiO_x/CsFAMA/$PC_{61}BM$/BCP/Ag formation process

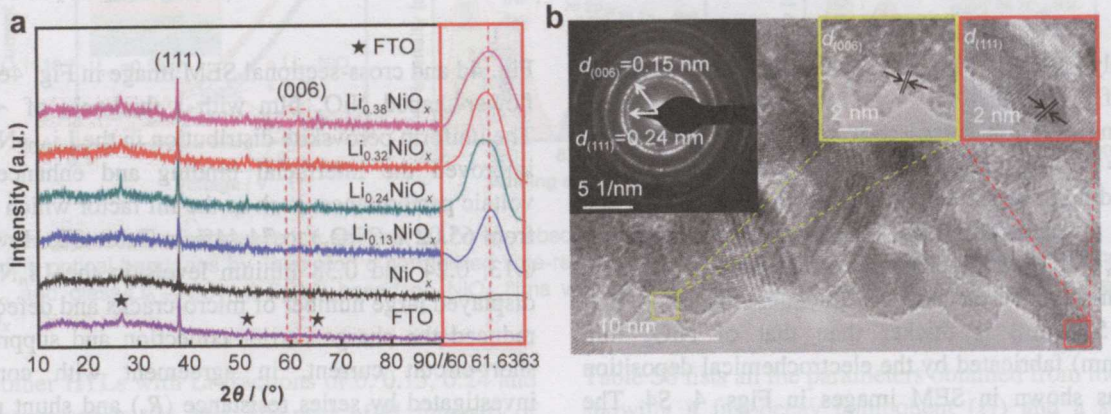

Fig. 2 **a** XRD patterns of Li_nNiO_x (n = 0, 0.13, 0.24, 0.32, 0.38; $0 < x \le 3$) film on FTO glass and enlarged peaks of (006) lattice plane in right segment; **b** HRTEM images and SAED pattern of $Li_{0.32}NiO_x$ nanocrystals

Li_nNiO_x ($0 \le n \le 1$; $0 < x \le 3$; cubic unit cell) [35], respectively. The intensity and position of the (111) peaks are almost identical for both NiO_x and Li_nNiO_x [36]. The ionic radius of Li (0.072–0.076 nm) is close to Ni (0.069–0.074 nm) [24, 25, 37, 38], which explaines why the (111) peak intensity of XRD pattern is not obviously shifted. The 2θ value for the (006) diffraction peak of Li_nNiO_x ($0 \le n \le 1$; $0 < x \le 3$) films in Fig. 2a shifted from 61.63° to 61.76° as the Li proportion increased from n = 0.32 to 0.38. The full width at half maximum (FWHM) of XRD peak at 60°–63° and corresponding (006) crystal plane spacing are displayed in Fig. S1b.

FWHM for $Li_{0.32}NiO_x$ (1.18°) is 0.09° and 0.52° smaller than that of $Li_{0.24}NiO_x$ (1.27°) and $Li_{0.38}NiO_x$ (1.70°), respectively. The corresponding crystal plane (006) spacing of 0.15110 nm of $Li_{0.32}NiO_x$ is maximum, comparative to 0.15086 nm of $Li_{0.24}NiO_x$ and 0.15078 nm of $Li_{0.38}NiO_x$. The smaller FWHM and enlarged lattice parameters improve the crystallinity [34]. Inductively coupled plasma-optical emission spectroscopy (ICP-OES) measurements showed that the lithium was doped in the nickel oxide successfully, as indicated in Table S1. The crystal plane spacings of (006) and (111) of $Li_{0.32}NiO_x$ were determined from high-resolution transmission electron microscopy (HRTEM) image and selected area electron diffraction (SAED) pattern, as shown in Fig. 2b, and the crystal plane spacing was calculated as the strong diffraction fringes matched well with XRD pattern shown in Fig. 2a, indicating that Li ions were successfully and controllably inserted into NiO_x ($0 < x \le 3$).

Enhanced photovoltaic performance for the representative perovskite solar cell with Li_nNiO_x (n = 0, 0.13, 0.24, 0.32, 0.38; $0 < x \le 3$) as HTL is shown in Figs. 3a, S2 and Table S2. With the lithium content increasing to 0.32, the current density (J_{SC}) and PCE reached the highest values of 26.53 mA·cm^{-2} and 20.44%, respectively. As the lithium content increased to 0.38 in $Li_{0.38}NiO_x$ ($0 < x \le 3$), the PCE of $Li_{0.38}NiO_x$ decreased. To verify the performance stability and high J_{SC} repeatability, the 10 groups of statistic best PCE and J_{SC} for the $Li_{0.32}NiO_x$-based PSC are shown in Fig. 3b and Table S3. The average PCE and J_{SC} are 19.4% ± 1.04% and (26.205 ± 1.14) mA·cm^{-2}, respectively. The average photovoltaic parameters of NiO_x, $Li_{0.13}NiO_x$, $Li_{0.24}NiO_x$ and $Li_{0.38}NiO_x$ are displayed in Tables S4-S7, respectively. The long-term air stabilities of unencapsulated $Li_{0.32}NiO_x$-based PSC are illustrated in Fig. 3c. The $Li_{0.32}NiO_x$-based device maintained average 75%, 90%, 80% and 98% of its initial PCE, J_{SC}, fill factor (FF), and open circuit voltage (V_{oc}),

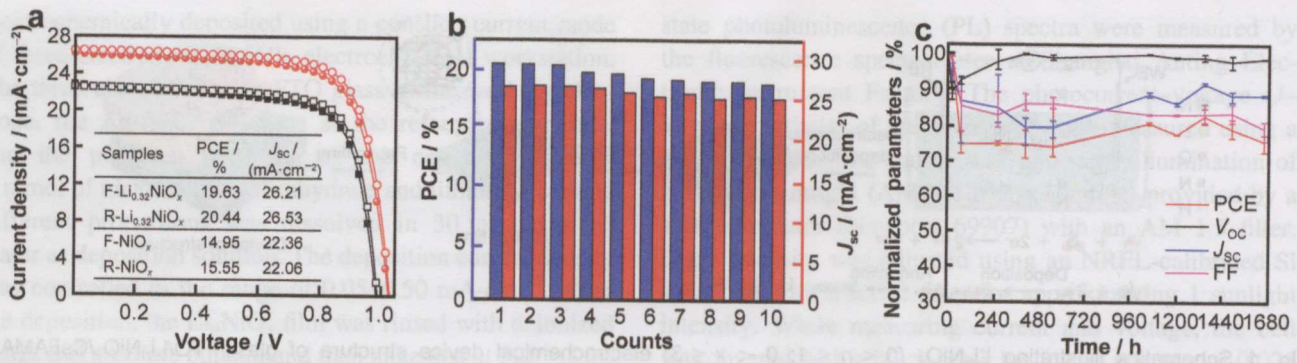

Fig. 3 **a** Current–density versus voltage (*J-V*) curves of PSC; **b** 10 groups of statistic champion PCE and J_{sc} for $Li_{0.32}NiO_x$-based PSC; **c** stability testing of photovoltaic performance for unencapsulated perovskite solar devices employing $Li_{0.32}NiO_x$ as hole-transfer materials

respectively, after 1656 h (69 days), suggesting the high stability of V_{OC} and J_{SC}.

Scanning electron microscopy (SEM) images of Li_n-NiO_x (n = 0, 0.13, 0.24, 0.32, 0.38; $0 < x \leq 3$) films and corresponding perovskite films are shown in Figs. 4, S3 and S4. The average pore size of a hierarchical porous $Li_{0.32}NiO_x$ film (~86.7 nm) was smaller than that of NiO_x (~224.5 nm); nevertheless, the thickness of $Li_{0.32}NiO_x$ film (~152.9 nm) is thicker than that of NiO_x film (~149.3 nm) fabricated by the electrochemical deposition method, as shown in SEM images in Figs. 4, S4. The doping of lithium ions increases the film thickness and decreases the pore sizes constructed by growing interplanar spacing, in accordance with XRD pattern in Fig. 2a. The modal particle size (consisting of 33.3% of the particles) of perovskite film of $Li_{0.32}NiO_x$ ranging from 300 to 350 nm is shown in Fig. 4c, which is larger than that of pure NiO_x substrate (250–300 nm) shown in Fig. 4f. SEM image in Fig. 4d and cross-sectional SEM image in Fig. 4e show the flower-shaped NiO_x film with a thickness of ~100 nm. The uniform perovskite distribution in the $Li_{0.32}NiO_x$ HTM improved the interfacial binding and enhanced photovoltaic performance, such as the fill factor which increased from 65.02% (NiO_x) to 74.44% in Table S2. However, the 0.13, 0.24 and 0.38 lithium levels in the Li_nNiO_x films displayed large number of micro-cracks and defects, which reduced the charge carrier collection and suppressed the short-circuit current, in agreement with conductivity investigated by series resistance (R_s) and shunt resistance (Rs_h) in the *J–V* measurement in Fig. S2 and Table S2.

The effective photovoltaic exciton-quenching was performed by steady-state photoluminescence (PL) in Figs. 5a, S6a. The ultraviolet–visible spectrum and the corresponding bandgaps for perovskite films on $Li_{0.32}NiO_x$ and NiO_x ($0 < x \leq 3$) substrate are shown in Figs. 5b, S5. The perovskite layer on $Li_{0.32}NiO_x$ exhibits a higher quenching

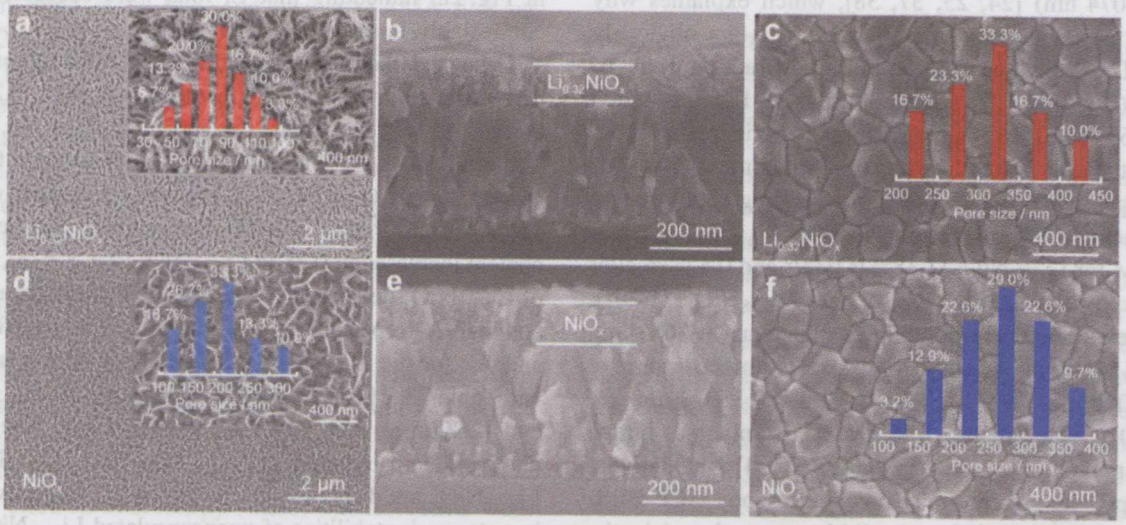

Fig. 4 Morphology of electrochemical deposition of hole transport layer: **a** SEM image and pore-size distribution, **b** cross-sectional SEM image of $Li_{0.32}NiO_x$ ($0 < x \leq 3$), and **c** SEM image of perovskite nanocrystals on $Li_{0.32}NiO_x$ film and grain-size distribution, **d** SEM image and pore-size distribution, **e** cross-sectional SEM image of NiO_x, and **f** SEM image of perovskite nanocrystals on NiO_x film and grain-size distribution

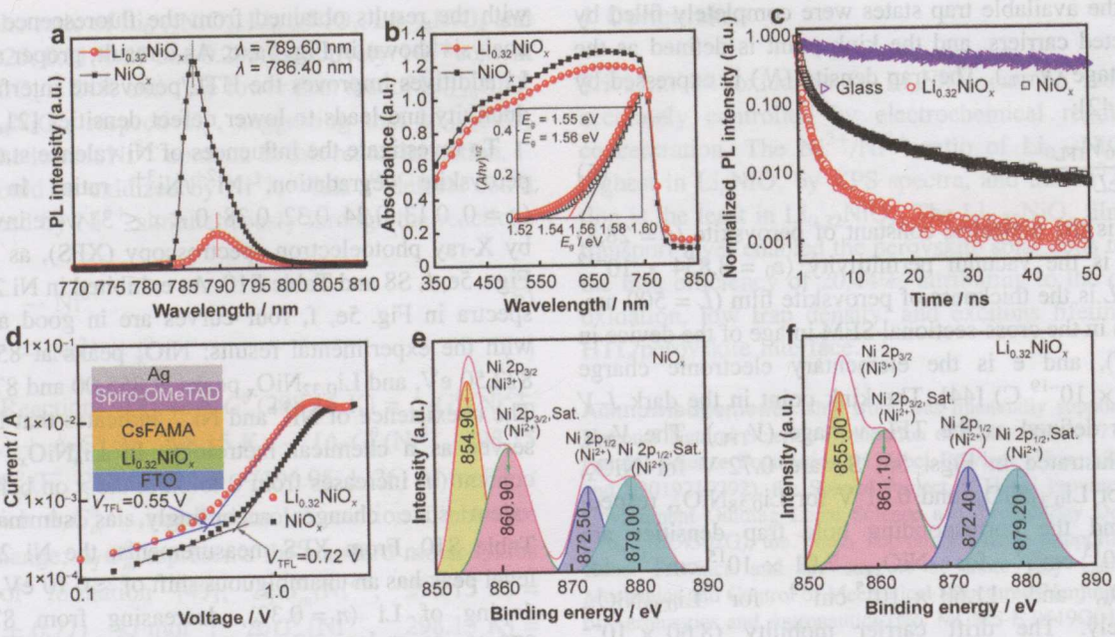

Fig. 5 **a** Steady-state photoluminescence spectra; **b** UV–Vis absorbance spectra of perovskite on NiO_x and $Li_{0.32}NiO_x$ and (inset) corresponding optical bandgaps by Tauc plot; **c** normalized time-resolved photoluminescence intensity of perovskite films on glass, glass/NiO_x, and glass/$Li_{0.32}NiO_x$; **d** SCLC based on NiO_x films without and with 0.32 Li additives; XPS spectra of **e** NiO_x and **f** $Li_{0.32}NiO_x$

rate than other HTLs with Li fractions of 0, 0.13, 0.24 and 0.38, as shown in Figs. 5a, S6a. The peak of PL intensity of $Li_{0.32}NiO_x$ is ~789.60 nm in accordance with its UV–Vis spectrum. The abnormal PL peak of perovskite on NiO_x HTL in Fig. 5a results from the MA migration [39]. The bandgap of perovskite can be tuned from 1.551 to 1.563 eV by changing Li content (n) in Li_nNiO_x, suggesting that the lower bandgap is conducive to photovoltaics.

The light absorbance of perovskite on $Li_{0.32}NiO_x$ film in Figs. 5b, S5b is lower than that of NiO_x film. This difference suggests that by sacrificing the light absorbance, a larger exciton-quenching as well as highly efficient PSC can be achieved. As shown in Figs. S5c, S6a, thanks to the $Li_{0.32}NiO_x$ hole-transfer layer with narrower bandgap and higher PL quenching efficiency, the $Li_{0.32}NiO_x$-based device obtained the highest PCE of 20.44% in Figs. 3, S2 and Table S2.

To consolidate our analysis, time-resolved photoluminescence (TRPL) spectroscopy was further employed to investigate the early interfacial charge separation kinetics of the $Li_{0.32}NiO_x$ hole-transfer layer and perovskite layer. The TRPL responses obtained by exciting at 400 nm shown in Figs. 5c, S6b for perovskite films on NiO_x hole transport layer with and without lithium can be fitted using a bi-exponential equation [40]:

$$f(t) = \sum_i A_i \exp(-t/\tau_i) + C \tag{3}$$

where A_i is the decay amplitude, t is time, τ_i is the decay time constant, and C is a constant for the baseline offset. Table S8 lists all the parameters obtained from the analysis, showing a fast-decay component (τ_1) and a slow-decay component (τ_2), with a weighted average:

$$\tau_{ave} = \frac{\sum A_i \tau_i^2}{\sum A_i \tau_i} \tag{4}$$

The perovskite film on NiO_x HTL had an average decay time of 7.09 ns. The decay time was significantly reduced (by 86.6%) to 0.95 ns when the perovskite film was coated on the $Li_{0.32}NiO_x$ substrate, implying faster charge transfer from perovskite film coated on $Li_{0.32}NiO_x$. The decay amplitude A_2 and longer decay time constant τ_2 of perovskite on the $Li_{0.32}NiO_x$ substrate were 16.45% and 10.22 ns, respectively, in contrast with A_1 and τ_1 of 83.55% and 0.90 ns, as shown in Table S8. The radiative recombination (16.45%) of perovskite film on $Li_{0.32}NiO_x$ substrate is lower than nonradiative recombination (83.55%), suggesting the low interfacial trap density. This is beneficial for short-circuit current (J_{SC}) and is consistent with device performance results in Fig. 3a. The intrinsic hole mobility was studied by measuring the space-charge-limited-current testing (SCLC) [41], using the dark current–voltage characteristics for a hole-only device structure with FTO/Li_nNiO_x/perovskite/Spiro-OMTAD/Ag, as shown in Figs. 5d, S7. On the log–log plot, the first-order linear relationships represent the ohmic response of the devices at low bias voltages. At higher voltages, the current increased nonlinearly and transferred to the trap-filled limit (TFL) at the kink point. It could be concluded

that all the available trap states were completely filled by the injected carriers, and the kink point is defined as the TFL voltage (V_{TFL}). The trap density (N_t) is expressed by Eq. (5) [42]:

$$N_t = \frac{2\varepsilon\varepsilon_0 V_{TFL}}{eL^2} \quad (5)$$

where ε is the dielectric constant of perovskite (ε = 28.8) [43], ε_0 is the vacuum permittivity ($\varepsilon_0 = 8.854 \times 10^{-12}$ F·m^{-1}), L is the thickness of perovskite film (L = 500 nm, as shown in the cross-sectional SEM image of the device in Fig. S4f), and e is the elementary electronic charge (e = 1.6×10^{-19} C) [44]. The kink point in the dark J–V curves is defined as the TFL voltage (V_{TFL}). The V_{TFL} values illustrated in Figs. 5d, S7 are 0.72 V for NiO_x, 0.55 V for $Li_{0.32}NiO_x$, and 0.91 V for $Li_{0.38}NiO_x$, respectively, and the corresponding hole trap densities are 9.18×10^{15} cm^{-3} for NiO_x, 7.01×10^{15} cm^{-3} for $Li_{0.32}NiO_x$, and 11.60×10^{15} cm^{-3} for $Li_{0.38}NiO_x$, respectively. The drift carrier mobility (8.60×10^{-2} cm^2·V^{-1}·S^{-1}) for $Li_{0.32}NiO_x$ is the largest in contrast to that of NiO_x (2.20×10^{-3} cm^2·V^{-1}·S^{-1}), $Li_{0.13}NiO_x$ (1.14×10^{-2} cm^2·V^{-1}·S^{-1}), $Li_{0.24}NiO_x$ (2.69×10^{-2} cm^2·V^{-1}·S^{-1}), and $Li_{0.38}NiO_x$ (7.15×10^{-2} cm^2·V^{-1}·S^{-1}), as shown in Table S9. These results indicate that the mean trap density of the HTL/perovskite interface can be significantly reduced by doping n = 0.32 in Li_nNiO_x HTL, which is expected to inhibit carrier recombination and promote J_{SC} in the corresponding solar cells, consistent with the results obtained from the fluorescence spectrum analysis shown in Fig. 5a, c. As a result, proper amount of Li additives improves the HTL/perovskite interfacial conductivity and leads to lower defect densities [21, 45, 46].

To investigate the influences of Ni valence states on the perovskite degradation, Ni^{2+}/Ni^{3+} ratios in Li_nNiO_x (n = 0, 0.13, 0.24, 0.32, 0.38; $0 < x \leq 3$) were investigated by X-ray photoelectron spectroscopy (XPS), as shown in Figs. 5e, f, S8 and Table S10. As exhibited in Ni $2p_{3/2}$ XPS spectra in Fig. 5e, f, four curves are in good agreement with the experimental results: NiO_x peaks at 854.90 and 872.50 eV, and $Li_{0.32}NiO_x$ peaks at 855.00 and 872.40 eV. The coexistence of $Ni^{3+}$and Ni^{2+} indicates that NiO_x film serves as a chemical metrology. In Li_nNiO_x, when Li content (n) increases from 0 to 0.38, the x on behalf of Ni valent state changes accordingly, as summarized in Table S10. From XPS measurements, the Ni $2p_{1/2}$ core level peak has an unambiguous shift of ≈0.10 eV, after the doping of Li (n = 0.32), decreasing from 872.50 to 872.40 eV (Fig. 5e, f). Li doping can significantly shift the valence band of NiO_x downward, suggesting occurrence of electron transfer and in agreement with the phenomena of a valence band shift [47]. No additional or new chemical components were detected by XPS except the Li signal shown in Fig. S8a and ICP-OES in Table S1, and the schematic band diagrams of the NiO_x/perovskite interface in the PSCs are illustrated in Fig. 6.

Ni^{2+} and Ni^{3+} concentration analysis of Li_nNiO_x from XPS spectra is summarized in Table S10. $Ni^{3+}/(Ni^{2+}$ +

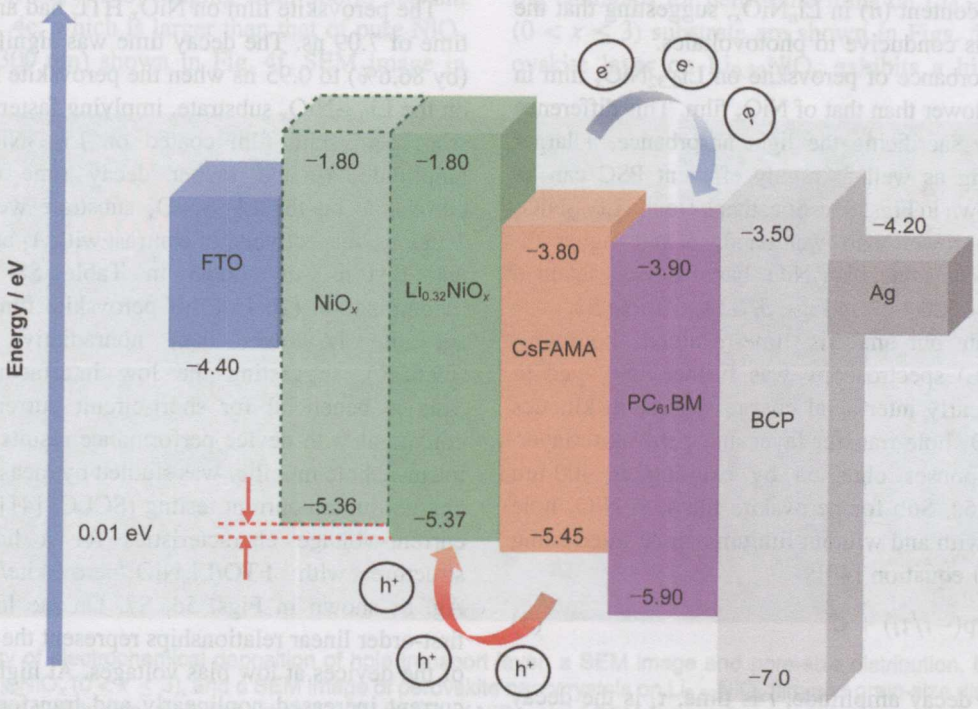

Fig. 6 Schematic illustration of energy band diagram of FTO/$Li_{0.32}NiO_x$/CsFAMA/$PC_{61}BM$/BCP/Ag perovskite solar cells

Ni^{3+}) molar ratio of $Li_{0.32}NiO_x$, $Li_{0.38}NiO_x$, $Li_{0.24}NiO_x$ and NiO_x is 0.25, 0.31, 0.29 and 0.29, respectively. Ni^{3+}content of $Li_{0.32}NiO_x$ is 24% and 16% lower than that of $Li_{0.38}NiO_x$ and $Li_{0.24}NiO_x$, respectively, suggesting that $Li_{0.32}NiO_x$ exhibits the lowest Ni^{3+} content. In this redox transition, I^- defects could be oxidized by Ni^{3+}, while I^0 defects could be produced by Ni^{3+} simultaneously through the reactions [48]:

$$Ni^{3+} + e^- \rightarrow Ni^{2+} \quad (6)$$

$$Ni^{3+} + I^- \rightarrow Ni^{2+} + I^0 \quad (7)$$

For Reaction (7), $\Delta_r G_m^\theta(298.15\ K) = \Delta_f G_m^\theta(Ni^{2+}, 298.15\ K) + \Delta_f G_m^\theta(I^0, 298.15\ K) - [\Delta_f G_m^\theta(Ni^{3+}, 298.15\ K) + \Delta_f G_m^\theta(I^-, 298.15\ K)] = -(196.05 \pm 26)\ kJ \cdot mol^{-1} < 0$, in which $\Delta_r G_m^\theta$ is standard molar reaction Gibbs free energy change; $\Delta_f G_m^\theta$ represents the standard molar Gibbs energy of formation [49]; $\Delta_f G_m^\theta(Ni^{2+}, 298.15\ K) = -(45.77 \pm 0.77)\ kJ \cdot mol^{-1}$; $\Delta_f G_m^\theta(Ni^{3+}, 298.15\ K) = (202 \pm 26)\ kJ \cdot mol^{-1}$; $\Delta_f G_m^\theta(I^-, 298.15\ K) = -(51.72 \pm 1.12)\ kJ \cdot mol^{-1}$; and $\Delta_f G_m^\theta(I^0, 298.15\ K) = 0\ kJ \cdot mol^{-1}$. Scientific spontaneity means that the Gibbs free energy change of the reaction is negative [50]. The Gibbs energy change $\Delta_r G_m^\theta(298.15\ K)$ of Reaction (5) is $(-45.77 + 0 - 202 + 51.72) = -196.05\ kJ \cdot mol^{-1} < 0$, suggesting that Reaction (5) occurs spontaneously, and Ni^{3+} oxidation of I^- leads to the degradation of perovskite. Low Ni^{3+} proportion in Li_nNiO_x HTL diminish the detrimental effects of halide in perovskite film.

The best photovoltaic performance using $Li_{0.32}NiO_x$ as HTL can be attributed to the high-quality $Li_{0.32}NiO_x$/perovskite interface and high charge carrier transport. The highest photocurrent and efficiency with perovskite on $Li_{0.32}NiO_x$ film manifest as follows. (1) The lattice constant is increased by Li atom substituting Ni vacancy in NiO_x framework, and $Li_{0.32}NiO_x$ pattern displays the highest crystallinity, as shown in XRD patterns. (2) The photogenerated excitons (electron hole pair) in $Li_{0.32}NiO_x$ /perovskite interface can be separated effectively, and excellent electrical conductivity of $Li_{0.32}NiO_x$ ensured the high-speed carriers transport, as exhibited in PL and TRPL spectra. (3) The $Li_{0.32}NiO_x$ hole trap density is the lowest as investigated in SCLC. (4) Compared to $Li_{0.38}NiO_x$ and $Li_{0.24}NiO_x$, the lower ratio of Ni^{3+} in $Li_{0.32}NiO_x$ reduces the oxidation of I^-. The low trap density and high photocurrent suggest that decreasing Ni^{3+} content reduces the oxidation and degradation of the perovskite in the HTL/perovskite interface [39]. Overall, through the electrochemical deposition method, $Li_{0.32}NiO_x$ is constructed with uniform 90-nm pore-size structure, high crystallinity, tunable Ni oxidation, and excellent photocurrent properties.

4 Conclusion

Trivalent Ni oxidation in Li_nNiO_x can be readily and accurately controlled by electrochemical regulating Li concentration. The Ni^{2+}/Ni^{3+} ratio of $Li_{0.32}NiO_x$ is the highest in Li_nNiO_x by XPS spectra, and the Ni^{3+} proportion is the least in $Li_{0.32}NiO_x$. The $Li_{0.32}NiO_x$ film as hole transport layer enabled the perovskite solar cells to acquire the best efficiency of 20.44%, attributing to the decreased oxidation, low trap density, and excitons lifetime in the HTL/perovskite interface.

Acknowledgements This work was financially supported by the National Natural Science Foundation of China (No. 11772207), the Natural Science Foundation of Hebei Province (Nos. A2019210204 and E2019210292), the Special Project of Hebei Provincial Central Government Guiding Local Science and Technology Development (No. 216Z4302G), the Youth Top-notch Talents Supporting Plan of Hebei Province and the support of State Key Laboratory of Mechanics and Control of Mechanical Structures, Nanjing University of Aeronautics and Astronautics (No. MCMS-E-0519G04).

Declarations

Conflicts of interests The authors declare that they have no conflict of interests.

References

[1] Kojima A, Teshima K, Shirai Y, Miyasaka T. Organometal halide perovskites as visible-light sensitizers for photovoltaic cells. J Am Chem Soc. 2009;131(17):6050.

[2] Chang JH, Liu K, Lin SY, Yuan YB, Zhou CH, Yang JL. Solution-processed perovskite solar cells. J Cent South Univ. 2020;27(4):1104.

[3] Chen W, Wu Y, Yue Y, Liu J, Zhang W, Yang X, Chen H, Bi E, Ashraful I, Grätzel M. Efficient and stable large-area perovskite solar cells with inorganic charge extraction layers. Science. 2015;350(6263):944.

[4] Wang L, Zhou H, Hu J, Huang B, Sun M, Dong B, Zheng G, Huang Y, Chen Y, Li L. A Eu^{3+}-Eu^{2+} ion redox shuttle imparts operational durability to Pb-I perovskite solar cells. Science. 2019;363(6424):265.

[5] Wang S, Jiang Y, Juarez-Perez EJ, Ono LK, Qi Y. Accelerated degradation of methylammonium lead iodide perovskites induced by exposure to iodine vapour. Nat Energy. 2016;2(1):16195.

[6] Raga SR, Jung MC, Lee MV, Leyden MR, Kato Y, Qi Y. Influence of air annealing on high efficiency planar structure perovskite solar cells. Chem Mater. 2015;27(5):1597.

[7] Li Y, Xu X, Wang C, Ecker B, Yang J, Huang J, Gao Y. Light-induced degradation of $CH_3NH_3PbI_3$ hybrid perovskite thin film. J Phys Chem C. 2017;121(7):3904.

[8] McGettrick JD, Hooper K, Pockett A, Baker J, Troughton J, Carnie M, Watson T. Sources of Pb (0) artefacts during XPS analysis of lead halide perovskites. Mater Lett. 2019;251:98.

[9] Xie H, Liu X, Lyu L, Niu D, Wang Q, Huang J, Gao Y. Effects of precursor ratios and annealing on electronic structure and surface composition of $CH_3NH_3PbI_3$ perovskite films. J Phys Chem C. 2016;120(1):215.

[10] Liu Z, Hu J, Jiao H, Li L, Zheng G, Chen Y, Huang Y, Zhang Q, Shen C, Chen Q. Chemical reduction of intrinsic defects in thicker heterojunction planar perovskite solar cells. Adv Mater. 2017;29(23):1606774.
[11] Mali SS, Kim H, Kim HH, Shim SE, Hong CK. Nanoporous p-type NiO_x electrode for p-i-n inverted perovskite solar cell toward air stability. Mater Today. 2018;21(5):483.
[12] Chen W, Zhou YC, Wang LJ, Wu YH, Tu B, Yu BB, Liu FZ, Tam HW, Wang G, Djurišić AB, Huang L, He ZB. Molecule-doped nickel oxide: verified charge transfer and planar inverted mixed cation perovskite solar cell. Adv Mater. 2018; 30(20):1800515.
[13] Ge B, Qiao HW, Lin ZQ, Zhou ZR, Chen AP, Yang S, Hou Y, Yang HG. Deepening the valance band edges of NiO_x contacts by alkaline earth metal doping for efficient perovskite photovoltaics with high open-circuit voltage. SOL RRL. 2019;3(8): 1900192.
[14] Ge B, Lin ZQ, Zhou ZR, Qiao HW, Chen AP, Hou Y, Yang S, Yang HG. Boric acid mediated formation and doping of NiO_x layers for perovskite solar cells with efficiency over 21%. SOL RRL. 2021;5(4):2000810.
[15] Zhang WN, Song J, Wang D, Deng KM, Wu JH, Zhang L. Dual interfacial modification engineering with P-type NiO nanocrystals for preparing efficient planar perovskite solar cells. J Phys Chem C. 2018;6(47):13034.
[16] Tang J, Jiao D, Zhang L, Zhang XZ, Xu X, Yao C, Wu JH, Zhang L. High-performance inverted planar perovskite solar cells based on efficient hole-transporting layers from well-crystalline NiO nanocrystals. Sol Energy. 2018;161:100.
[17] Park JH, Seo J, Park S, Shin SS, Kim YC, Jeon NJ, Shin HW, Ahn TK, Noh JH, Yoon SC. Efficient $CH_3NH_3PbI_3$ perovskite solar cells employing nanostructured P-type NiO electrode formed by a pulsed laser deposition. Adv Mater. 2015;27(27): 4013.
[18] Zhang BJ, Su J, Guo X, Zhou L, Lin ZH, Feng LP, Zhang JC, Chang JJ, Hao Y. NiO/perovskite heterojunction contact engineering for highly efficient and stable perovskite solar cells. Adv Sci. 2020;7(11):1903044.
[19] Juybari HA, Bagheri-Mohagheghi MM, Shokooh-Saremi M. Nickel–lithium oxide alloy transparent conducting films deposited by spray pyrolysis technique. J Alloy Compd. 2011;509(6): 2770.
[20] Corani A, Li MH, Shen PS, Chen P, Guo TF, El Nahhas A, Zheng K, Yartsev A, Sundström V, Ponseca CS. Ultrafast dynamics of hole injection and recombination in organometal halide perovskite using nickel oxide as P-type contact electrode. J Phys Chem Lett. 2016;7(7):1096.
[21] Cheng Y, Li M, Liu X, Cheung SH, Chandran HT, Li HW, Xu X, Xie YM, So SK, Yip HL. Impact of surface dipole in NiO_x on the crystallization and photovoltaic performance of organometal halide perovskite solar cells. Nano Energy. 2019;61:496.
[22] Rambau B, Ramasastry C, Chowdari BVR. Radiation damage studies of Co^{2+} and Ni^{2+} doped NH_4Cl crystals. Phys Status Solidi B. 1983;118(1):381.
[23] Hou Y, Tang LJ, Qiao HW, Zhou ZR, Zhong YL, Zheng LR, Chen MJ, Yang S, Yang HG. Ni-Co-O hole transport materials: gap sates assisted hole extraction with superior electrical conductivity. J Mater Chem A. 2019;7(36):20905.
[24] Yin X, Guo Y, Xie H, Que W, Kong LB. Nickel oxide as efficient hole transport materials for perovskite solar cells. SOL RRL. 2019;3(5):1900001.
[25] Srinivas C, Tirupanyam BV, Satish A, Seshubai V, Sastry DL, Caltun OF. Effect of Ni^{2+} substitution on structural and magnetic properties of Ni–Zn ferrite nanoparticles. J Magn Magn Mater. 2015;382:15.
[26] Thakur UK, Kumar P, Gusarov S, Kobryn AE, Riddell S, Goswami A, Kazi M, Alam KM, Savela S, Kar P, Thundat T, Meldrum A, Shankar K. Consistently high V_{oc} values in p-i-n type perovskite solar cells using Ni^{3+}-doped NiO nanomesh as the hole transporting layer. ACS Appl Mater. 2020;12(10): 11467.
[27] Traore B, Pedesseau L, Blancon J, Tretiak S, Mohite AD, Even J, Katan C, Kepenekian M. Importance of vacancies and doping in the hole-transporting nickel oxide interface with halide perovskites. ACS Appl Mater Interf. 2020;12(5):6633.
[28] Qiu Z, Gong H, Zheng G, Yuan S, Zhang H, Zhu X, Zhou HP, Cao BQ. Enhanced physical properties of pulsed laser deposited NiO films via annealing and lithium doping for improving perovskite solar cell efficiency. J Mater Chem C. 2017;5(28):7084.
[29] Lee SW, Gallant BM, Byon HR, Hammond PT, Shao-Horn Y. Nanostructured carbon-based electrodes: bridging the gap between thin-film lithium-ion batteries and electrochemical capacitors. Energy Environ Sci. 2011;4(6):1972.
[30] Subbiah AS, Halder A, Ghosh S, Mahuli N, Hodes G, Sarkar SK. Inorganic hole conducting layers for perovskite-based solar cells. J Phys Chem Lett. 2014;5(10):1748.
[31] Wu MS, Yang CH, Wang MJ. Morphological and structural studies of nanoporous nickel oxide films fabricated by anodic electrochemical deposition techniques. Electrochim Acta. 2008; 54(2):155.
[32] Girolamo DD, Matteocci F, Piccinni M, Carlo AD, Dini D. Anodically electrodeposited NiO nanoflakes as hole selective contact in efficient air processed p-i-n perovskite solar cells. Sol Energy Mater Sol Cells. 2020;205:110288.
[33] Zhao J, Chen H, Shi J, Gu J, Dong X, Gao J, Ruan M, Yu L. Electrochemical and oxygen desorption properties of nanostructured ternary compound Na_xMnO_2 directly templated from mesoporous SBA-15. Microporous Mesoporous Mat. 2008; 116(1–3):432.
[34] Wu CC, Yang CF. Fabricate heterojunction diode by using the modified spray pyrolysis method to deposit nickel–lithium oxide on indium tin oxide substrate. ACS Appl Mater Interf. 2013; 5(11):4996.
[35] Zhang BP, Zhang YR, Dong Y, Li JF, Chen C. Effect of Li content on microstructure and dielectric properties of $Li_xTi_yNi_{1-x-y}O$ thin films. Ferroelectrics. 2007;357(1):92.
[36] Saki Z, Kári S, Boschloo G, Taghavinia N. The effect of lithium doping in solution: processed nickel oxide films for perovskite solar cells. Chem Phys Chem. 2019;20(24):3322.
[37] Liu K, Liu Y, Zhu HF, Dong XL, Wang YG, Wang CX, Xia YY. $NaTiSi_2O_6$/C composite as a novel anode material for lithium-ion batteries. Acta Phys Chim Sin. 2020;36(11):1912030.
[38] Jin X, Xu Q, Liu H, Yuan X, Xia Y. Excellent rate capability of Mg doped Li $[Li_{0.2}Ni_{0.13}Co_{0.13}Mn_{0.54}]O_2$ cathode material for lithium-ion battery. Electrochim Acta. 2014;136:19.
[39] Gao XX, Luo W, Zhang Y, Hu R, Zhang B, Züttel A, Feng Y, Nazeeruddin MK. Stable and high–efficiency methylammonium-free perovskite solar cells. Adv Mater. 2020;32(9): 1905502.
[40] He J, Zhao J, Shen T, Hidaka H, Serpone N. Photosensitization of colloidal titania particles by electron injection from an excited organic dye–antennae function. J Phys Chem B. 1997;101(44): 9027.
[41] Dong Q, Fang Y, Shao Y, Mulligan P, Qiu J, Cao L, Huang J. Electron-hole diffusion lengths > 175 μm in solution-grown $CH_3NH_3PbI_3$ single crystals. Science. 2015;347(6225):967.
[42] Bube RH. Trap density determination by space-charge-limited currents. J Appl Phys. 1962;33(5):1733.
[43] Hang Y, Liu X, Li P, Duan Y, Hu X, Li F, Song Y. Dopamine-crosslinked TiO_2/perovskite layer for efficient and

photostable perovskite solar cells under full spectral continuous illumination. Nano Energy. 2019;56:733.

[44] Son DY, Kim SG, Seo JY, Lee SH, Shin H, Lee D, Park NG. Universal approach toward hysteresis-free perovskite solar cell via defect engineering. J Am Chem Soc. 2018;140(4):1358.

[45] Fang Z, He H, Gan L, Li J, Ye Z. Understanding the role of lithium doping in reducing nonradiative loss in lead halide perovskites. Adv Sci. 2018;5(12):1800736.

[46] Mao GP, Wang W, Shao S, Sun XJ, Chen SA, Li MH, Li HM. Correction to: research progress in electron transport layer in perovskite solar cells. Rare Met. 2020. https://doi.org/10.1007/s12598-020-01375-8.

[47] Guo Y, Jin Z, Yuan S, Zhao JS, Ai XC. Effects of interfacial energy level alignment on carrier dynamics and photovoltaic performance of inverted perovskite solar cells. J Power Sources. 2020;452:227845.

[48] Chen H, Motuzas J, Martens W, Diniz da Costa JC. Ceramic metal oxides with Ni^{2+} active phase for the fast degradation of orange II dye under dark ambiance. Ceram Int. 2018;44 (6): 6634.

[49] Gamsjäger H, Bugajski J, Gajda T, Lemire R, Preis W. Chemical Thermodynamics, North Holland Elsevier Science Publishers B. V. Amsterdam, The Netherlands, 2005; 89.

[50] Yang TY, Gregori G, Pellet N, Grätzel M, Maier J. The significance of ion conduction in a hybrid organic–inorganic lead-iodide-based perovskite photosensitizer. Angew Chem Int Ed. 2015;54(27):7905.